Thin–Walled Structures 215 (2025) 113504

Contents lists available at ScienceDirect

Thin-Walled Structures

journal homepage: www.elsevier.com/locate/tws

Full length article

Wrinkling of thin plates and shells on shrinking substrates

Tomo Veldin [a], Jonas Trojer [b], Boštjan Brank [a], Miha Brojan [b],*

[a] University of Ljubljana, Faculty of Civil and Geodetic Engineering, Jamova 2, SI-1000, Ljubljana, Slovenia

[b] University of Ljubljana, Faculty of Mechanical Engineering, Laboratory for Nonlinear Mechanics, Aškerčeva 6, SI-1000, Ljubljana, Slovenia

ARTICLE INFO

Keywords:
Wrinkling
Thin shell
Finite element
3D solid
Neo-Hookean material

ABSTRACT

A new finite element formulation and a set of novel desktop experiments for studying wrinkling of thin plates and shells on shrinking substrates is presented. In developing the computational model, we build on our previous work and further develop the finite element formulation by implementing a neo-Hookean material model to more accurately capture large displacements and large strains in the substrate. The substrate is discretized with solid 3D hexahedral 8 node finite elements, whose formulation was derived using the theory of incompatible modes. Our computational model is validated through a series of numerical and desktop experiments on plates and shells. Numerically, the strain mismatch is simulated by cooling the substrate, while experimentally it is achieved through the shrinkage of the silicone substrate during solidification, which was enhanced by the addition of a silicone oil. The extent of shrinkage was controlled by the volume ratio of silicone elastomer-to-silicone oil. A good agreement between the calculated wavelengths of the neighboring wrinkles from numerical simulations, experiments and theoretical predictions confirmed the predictive effectiveness of the proposed numerical procedure.

1. Introduction

Surface wrinkling induced by the shrinkage of the substrate is a phenomenon observed in various processes, such as aging skin, drying fruit, solidifying polymers, etc. This phenomenon occurs when a thin structure is adhered on a softer substrate that undergoes shrinkage as a result of cooling, evaporation, drying, curing, etc. As the substrate shrinks, the thin structure is forced to accommodate the reduction in size of the softer substrate, leading to localized deformation and the formation of distinctive surface patterns. This intricate interplay between the substrate and the thin structure is governed by the geometry, mismatch in their material properties and the amount of compressive stresses that exceed a certain threshold, after which it is energetically more efficient for an initially smooth structure to bend rather than compress further.

In practice, wrinkling was used to engineer functional and responsive surfaces with tailored properties, such as tunable microlens arrays [1], mimicking of natural gripping mechanisms through adhesion control [2], surface wetting control [3], aerodynamic drag control [4], opacity control [5], piezo-resistive sensors [6], biocompatible electronics, such as thin film transistors (TFT) [7] and OLEDs [8], microfluidic electronics [9], artificial skin electronics [10], epidermal patches for the monitoring of metabolic biomarkers [11], monitoring of food ripening process [12] and bladder cancer cell detection [13,14].

Most of these applications were developed from experiments that relied on highly innovative approaches, but to really understand the process an accurate theoretical or computational simulation model is needed. The simulation can rely on commercial FEM software, such as Abaqus, Ansys or Comsol, (see, e.g. [15–18]) or can be performed with custom-built numerical algorithms (see e.g., [19–24]). The most notable progress in this direction was made by Stoop et al. [25], Xu and Potier-Ferry [26], Lavrenčič et al. [27], Veldin et al. [28,29], Zhao et al. [30] and Sriram et al. [31]. Lavrenčič et al. [27] used implicit dynamics with a high frequency energy dissipating algorithm [32–34]. Xu and Potier-Ferry [26] approached the problem with a nonlinear 7-parameter 3D shell element with reduced integration [35,36] and an 8-node linear 3D solid finite element for the substrate, also with reduced integration. Veldin et al. [28] used the reduced Kirchhoff–Love shell model to define a discrete Kirchhoff quadrilateral finite element, named DKQ-3, coupled to a Winkler foundation. In a subsequent study Veldin et al. [29] developed a 5 degree-of-freedom discrete Kirchhoff–Love non-linear quadrilateral finite element, based on the bilinear Coons patch, also using the Winkler foundation. Zhao et al. [30] extended the Fourier spectral method, previously used by Huang et al. [37–39] on planar film–substrate systems, to curved bilayer systems. Sriram et al. [31] used an energy minimization procedure obtained from a variational framework implemented through a Q_1RT_0 finite element using Raviart–Thomas-type interpolations.

* Corresponding author.
E-mail address: miha.brojan@fs.uni-lj.si (M. Brojan).

https://doi.org/10.1016/j.tws.2025.113504
Received 14 January 2025; Received in revised form 24 April 2025; Accepted 22 May 2025
Available online 7 June 2025

However, not many researchers performed both numerical and experimental analyses. One of them was Cao et al. [40] who compared experiments on microscopic spheres with a numerical study in Abaqus, and Stoop et al. [25] who compared wrinkle patterns obtained on polymeric spheres to numerical solutions of a generalized Swift-Hohenberg fourth-order theory using their own finite element code. Recently, Xu et al. [41] published a study on the stability of a hexagonal pattern on a buckled sphere, where they compared numerical results obtained using Abaqus with experimental observations. In their experiment, they fabricated hollow spheres, but instead of using the concept of a bilayer to achieve the initial surface wrinkling, they fabricated them with a hexagonal network of ridges already present in the undeformed configuration and observed its buckling upon subsequent shrinking of the sphere interior. Another recent study, by Zavodnik and Brojan [42] also focused on the theory, experiments and a new numerical pseudo-spectral method based on spherical harmonics that is remarkably successful in predicting wrinkling on spheres.

In this paper we present a new finite element formulation and a set of novel desktop experiments for the analysis of thin shell wrinkling on shrinking substrates. In the development of the computational model we build further on our previous work described in [28,43,44]. First, the substrate is modeled using a hexahedral 8-node solid finite element that is free from volumetric locking due to the application of incompatible modes [45]. This makes it particularly suitable for analyzing nearly incompressible hyperelastic materials. Second, we employ a neo-Hookean hyperelastic material model for both the substrate and the thin surface film, replacing the previously used St. Venant-Kirchhoff model. The neo-Hookean model more accurately captures large displacements and strains, overcoming the limitations of the St. Venant-Kirchhoff model, which produces erroneous results under compression due to its lack of polyconvexity. As for the shell finite element, we apply a fully non-linear Discrete-Kirchhoff shell finite element with 4 nodes [29]. It has rich interpolation of displacements, which allows to get smooth wrinkling patterns for relatively coarse meshes. The shell finite element has three global displacements and two local rotations at each node. Because of the fulfillment of the Kirchhoff kinematic constraint at the discrete points, the shell rotations and displacements are not independent (rather they are weakly coupled), which is advantageous when using solid and shell finite elements together (as is the case in this work). Namely, there is no need for an additional procedure to couple shell rotations with solid displacements. Equality of the shell and solid displacements at a common (solid-shell) node naturally includes coupling between the solid displacements and the shell rotations. In this sense, the coupling between the shell degrees of freedom and the solid degrees of freedom is guaranteed automatically.

Moreover, our model was applied to a range of both numerical and desktop experiments on flat (plate) as well as curved (shell) geometries. Numerically, the strain mismatch is simulated by cooling the substrate, while experimentally it is achieved through the shrinkage of the silicone substrate during solidification that was pronounced by the addition of a silicone oil. The extent of the shrinkage was controlled by the volume ratio of silicone elastomer to silicone oil.

The rest of the paper is organized as follows: in Section 2 all the computational models that were used are described, including the neo-Hookean material model applied to shells, the Kirchhoff–Love shell model and a 3D model together with its finite element implementation. In Section 3, the results of numerical simulations and experiments on rectangular and circular plates, and on cylindrical and hemispherical shells that are attached to thick substrates are discussed. In Section 4, a summary of our findings and insights into potential future extensions of our current research is presented.

2. Computational models

In this section the shell finite element is briefly described without going into too much detail. It is based on the DKQ-5 shell finite element, initially introduced in [29], which is upgraded here with a neo-Hookean material model, naming it DKQ-5_neo. We also describe the 3D hexahedral 8 node finite element that is based on a neo-Hookean material model, here named 3D_Solid_neo. It uses the theory of incompatible modes, which makes it less stiff. The aim of developing a 3D finite element is to be used to model thick, soft substrates more accurately.

2.1. Constitutive relations

First, general equations of the material model, which can be directly used in the formulations of 3D finite elements are introduced. The general material equations are further adjusted to the shell formulation, which is based on the plane stress assumption.

2.1.1. Neo-Hookean material model

The neo-Hookean material model is, in general, only available for 3D formulations. This material model is more appropriate than the mostly widely used Saint Venant–Kirchhoff material model for cases when compression prevails in the deformation field. The strain energy density function of the neo-Hookean material model is given by

$$W = C_1(\operatorname{tr}\boldsymbol{C} - 3 - 2\ln J) + D_1(J-1)^2, \tag{1}$$

where

$$C_1 = \frac{\mu}{2}, \quad D_1 = \frac{\lambda}{2} \quad \text{and} \quad J = \det(\boldsymbol{F}) \tag{2}$$

are material constants and determinant of the deformation gradient, respectively. In formulation (1), $\boldsymbol{C}$ represents the right Cauchy–Green deformation tensor,

$$\boldsymbol{C} = \boldsymbol{F}^T\boldsymbol{F}, \tag{3}$$

while the deformation gradient is considered in the form

$$\boldsymbol{F} = \boldsymbol{G} + \nabla\boldsymbol{u} \tag{4}$$

with $\boldsymbol{G}$ and $\nabla\boldsymbol{u}$ being the metric tensor of the undeformed shell and the displacement gradient, respectively.

Differentiation of Eq. (1) with respect to $\boldsymbol{C}$, yields the second Piola–Kirchhoff stress tensor

$$\boldsymbol{S} = 2\frac{\partial W}{\partial \boldsymbol{C}}. \tag{5}$$

Note that, the above equations are appropriate to be used within 3D formulations and are as such suitable for implementation in 3D finite elements.

2.1.2. Neo-Hookean constitutive material model for shells

There is no straightforward procedure to transform the basic neo-Hookean equations into a form suitable for the shell formulation. In the shell equations, where the plane stress field is assumed the stress in the direction $S^{33} = 0$. Because of this assumption, equations in Section 2.1.1 have to be appropriately modified. The S^{33} element of the second Piola–Kirchhoff stress must be zero, but this can only be fulfilled approximately, $S^{33} \approx 0$. This equation is nonlinear and, as such, should be solved iteratively by the Newton–Raphson method as described in [46]. Variables in Eq. (1) should be modified such that they are suitable for the use in the shell theory. Some useful relations that will be needed later are listed next. The determinant of the right Cauchy–Green deformation tensor can be expressed as

$$\det\boldsymbol{C} = \det(\boldsymbol{F}^T\boldsymbol{F}) = \det\boldsymbol{F}^T\det\boldsymbol{F} = J^2, \tag{6}$$

from which it follows

$$J = \sqrt{\det\boldsymbol{C}}. \tag{7}$$

The trace of $\boldsymbol{C}$ in Eq. (1) can be written as

$$\operatorname{tr}\boldsymbol{C} = C_{ij}\boldsymbol{G}^i\cdot\boldsymbol{G}^j = C_{\alpha\beta}\boldsymbol{G}^\alpha\cdot\boldsymbol{G}^\beta + C_{33}. \tag{8}$$

Deformations will be characterized with the Green–Lagrange deformation tensor $\boldsymbol{E} := (\boldsymbol{C} - \boldsymbol{G})/2$ (tensor $\boldsymbol{G}$ can be replaced with the unit tensor $\boldsymbol{I}$ when the Cartesian coordinate system is used). Tensor $\boldsymbol{C}$ can be therefore expressed as

$$\boldsymbol{C} = 2\boldsymbol{E} + \boldsymbol{G} = (2E_{ij} + G_{ij})\boldsymbol{G}^i \otimes \boldsymbol{G}^j \tag{9}$$

or the same in index notation

$$C_{ij} = 2E_{ij} + G_{ij}. \tag{10}$$

Since the deformation gradient $\boldsymbol{F}$ can be written as

$$\boldsymbol{F} = \boldsymbol{g}_i \otimes \boldsymbol{G}^i, \tag{11}$$

$\boldsymbol{C}$ can also be written as follows

$$\boldsymbol{C} = \boldsymbol{F}^T\boldsymbol{F} = g_{ij}\boldsymbol{G}^i \otimes \boldsymbol{G}^j. \tag{12}$$

In matrix notation with covariant and contravariant components this reads

$$(C_{ij}) = \begin{pmatrix} g_{11} & g_{12} & 0 \\ g_{21} & g_{22} & 0 \\ 0 & 0 & C_{33} \end{pmatrix} \quad \text{and} \quad (\overline{C}^{ij}) = \begin{pmatrix} g^{11} & g^{12} & 0 \\ g^{21} & g^{22} & 0 \\ 0 & 0 & C_{33}^{-1} \end{pmatrix}, \tag{13}$$

respectively.

In case when the Saint Venant–Kirchhoff material model is used, such as in [29], it is enough if the Gauss integration is only performed in two directions. However, when the neo-Hookean material model is used, one has to integrate in the direction of the shell thickness. At every Gauss integration point the Newton–Raphson method has to be used to fulfill the $S^{33} \approx 0$ condition.

According to Eq. (5) the following form of the second Piola–Kirchhoff stress tensor can now be obtained

$$\boldsymbol{S} = \mu(G^{ij} - \overline{C}^{ij})\boldsymbol{G}_i \otimes \boldsymbol{G}_j + \lambda(J^2 - J)\overline{C}^{ij}\boldsymbol{G}_i \otimes \boldsymbol{G}_j. \tag{14}$$

If it is assumed for very thin shells that the metric tensor is constant over the thickness of the shell, it follows that

$$G_{ij} \approx A_{ij}, \quad G^{ij} \approx A^{ij}. \tag{15}$$

Furthermore, one can take into account the following expressions: $A_{\alpha\beta} = \boldsymbol{A}_\alpha \cdot \boldsymbol{A}_\beta$, $A_{\alpha i} = A_{j\alpha} = A^{\alpha i} = A^{j\alpha} = 0$ and $A_{33} = A^{33} = 1$. Based on all these assumptions the following approximations can be used

$$C_{\alpha\beta} = g_{\alpha\beta} \approx a_{\alpha\beta}, \quad \overline{C}^{\alpha\beta} = g^{\alpha\beta} \approx a^{\alpha\beta}, \tag{16}$$

where $C_{33} \neq g_{33}$, as is defined in [46]. Therefore C_{ij} and $\overline{C}^{ij}$ are now

$$(C_{ij}) = \begin{pmatrix} a_{11} & a_{12} & 0 \\ a_{21} & a_{22} & 0 \\ 0 & 0 & C_{33} \end{pmatrix} \quad \text{and} \quad (\overline{C}^{ij}) = \begin{pmatrix} a^{11} & a^{12} & 0 \\ a^{21} & a^{22} & 0 \\ 0 & 0 & C_{33}^{-1} \end{pmatrix}. \tag{17}$$

With all the components of the tensor $\boldsymbol{C}$ at hand the terms which are included in the energy density function given by Eq. (1) can be evaluated. The second Piola–Kirchhoff stress tensor $\boldsymbol{S}$ can be reformulated into a more suitable form for the use with thin shells:

$$\boldsymbol{S} = \mu(A^{ij} - \overline{C}^{ij})\boldsymbol{A}_i \otimes \boldsymbol{A}_j + \lambda(J^2 - J)\overline{C}^{ij}\boldsymbol{A}_i \otimes \boldsymbol{A}_j. \tag{18}$$

As such, the S^{33} component is then

$$S^{33} = \mu(1 - C_{33}^{-1}) + \lambda(J^2 - J)C_{33}^{-1}. \tag{19}$$

Since $S^{33} \approx 0$, equations needed for the Newton–Raphson method can be written. This method needs an initial value of the variable, a function of this variable and the derivative of the function with respect to this variable. In our case this variable is C_{33} and the function is $S^{33}(C_{33})$. In the Ith iteration, the component $S^{33}(C_{33})$ of the stress function are written as S_I^{33}. A correction of the initial value ΔC_{33}^I in the Ith iteration is calculated as

$$\Delta C_{33}^I = \frac{S_I^{33}}{\frac{\partial S_I^{33}}{\partial C_{33}^I}}. \tag{20}$$

When this correction to the initial value C_{33}^I in the Ith iteration is added, a new value C_{33}^{I+1} for $(I+1)$-th iteration is obtained

$$C_{33}^{I+1} = C_{33}^I - \Delta C_{33}^I. \tag{21}$$

The new value for C_{33}^{I+1} is further inserted into S^{33}. With every iteration the value of S^{33} approaches 0. When S^{33} is close enough to 0, i.e. when it is smaller than the predefined error criterion, the iteration process stops. If that is not the case, the current value of the C_{33}^{I+1} is again inserted into Eq. (20) to get a better approximation. When the iteration procedure is finished, the membrane and bending forces can be calculated according to

$$N^{\alpha\beta} = \int_{-h/2}^{h/2} S^{\alpha\beta} \nu_g d\theta^3, \qquad M^{\alpha\beta} = \int_{-h/2}^{h/2} S^{\alpha\beta} \nu_g \theta^3 d\theta^3, \tag{22}$$

where integration is performed numerically.

2.2. Kirchhoff–Love shell model

The initial shell configuration is described as

$$\boldsymbol{R}(\xi^1, \xi^2, \xi^3) := \boldsymbol{X}(\xi^1, \xi^2) + \xi^3 \boldsymbol{A}_3(\xi^1, \xi^2), \tag{23}$$

where ξ^1 and ξ^2 are the convective curvilinear coordinates of the mid-surface, $\xi^3 \in [-h/2, h/2]$ is the through-the-thickness convective coordinate (h is the thickness), $\boldsymbol{X}$ is a vector field giving the position of the mid-surface and $\boldsymbol{A}_3$ is a unit mid-surface normal vector field. From here forward, the derivatives will be written in the shortened form as $(\ )_{,\alpha} = \partial(\ )/\theta^\alpha$, while the capital letters will denote objects of the initial configuration and small letters will denote objects in the deformed configuration.

As a strain measure, the Green–Lagrange strain tensor will be used

$$\boldsymbol{E} := \frac{1}{2}(\boldsymbol{g} - \boldsymbol{G}), \tag{24}$$

where $\boldsymbol{g}$ denotes the metric tensor of the deformed shell configuration s and $\boldsymbol{G}$ of the initial shell configuration S. Because of the Kirchhoff–Love kinematic assumption, the *structure* of the above kinematic expressions remains the same also for the deformed configuration. Taking this into account, one can write the covariant Green–Lagrange strain tensor components as

$$E_{\alpha\beta} = \epsilon_{\alpha\beta} + \xi^3\kappa_{\alpha\beta} + (\xi^3)^2\rho_{\alpha\beta}, \quad \text{and} \quad E_{i3} = 0, \tag{25}$$

where

$$\epsilon_{\alpha\beta} = \frac{1}{2}\left(a_{\alpha\beta} - A_{\alpha\beta}\right), \qquad \kappa_{\alpha\beta} = -(b_{\alpha\beta} - B_{\alpha\beta}), \qquad \rho_{\alpha\beta} = \frac{1}{2}\left(c_{\alpha\beta} - C_{\alpha\beta}\right). \tag{26}$$

Here, $B_{\alpha\beta} = -\boldsymbol{A}_\alpha \cdot \boldsymbol{A}_{3,\beta}$ is the initial curvature at the considered mid-surface point and $C_{\alpha\beta}$ is the third fundamental form also in the initial configuration. Following the usual approach, see e.g. [47], the effect of $\rho_{\alpha\beta}$ will also be neglected.

The displacement vector, which connects the deformed and initial configurations for Kirchhoff–Love shells, is defined as

$$\boldsymbol{U} = \boldsymbol{x} - \boldsymbol{X}. \tag{27}$$

For more details cf. [29].

2.2.1. Shell potential energy for neo-Hookean material model

Our DKQ-5 shell finite element [29] that is based on a Saint Venant–Kirchhoff material model is upgraded to a neo-Hookean material model. The new finite element is named DKQ-5_neo. In this way, the computational model is more physically accurate for problems involving larger compressive strains, since neo-Hookean does not exhibit nonphysical strain softening. The potential energy of this finite element is

$$\Pi^e(\boldsymbol{U}) = \int_{S^e} W(E_{ij})dV^e - \int_{M^e} \boldsymbol{U} \cdot \boldsymbol{p}\, dA^e. \tag{28}$$

Besides this equation an additional equation which imposes plane stress state is needed,

$$\frac{\partial W}{\partial E_{33}} = 0. \tag{29}$$

The strain energy density function $W(E_{ij})$ of the neo-Hookean material model is defined with Eq. (1) which is used to calculate the variation of Eq. (28)

$$\delta \Pi^e(\boldsymbol{U}, \delta \boldsymbol{U}) = \int_{S^e} \frac{\partial W}{\partial E_{ij}} \delta E_{ij} dV^e - \int_{M^e} \delta \boldsymbol{U} \cdot \boldsymbol{p} \, dA^e = 0. \tag{30}$$

As with the DKQ-5 finite element, DKQ-5_neo also requires numerical integration in the direction of the shell thickness. The functional in Eq. (28) also contains a volume integral which cannot be analytically evaluated with a neo-Hookean material model. However, it can be calculated with a 5-point Gauss integration rule in combination with the standard 3-point Gauss integration across the element thickness. This results in a 5×3 Gauss integration. The part of Eq. (28) relating to the external load can be calculated in the same way as with the DKQ-5 finite element, with a 5-point Gauss integration rule.

2.3. 3D model

The 3D model contains no special kinematic assumptions. It uses the Green–Lagrange strain tensor given in Eq. (24). Metric tensors in initial and deformed configurations are written as

$$\boldsymbol{G} := G_{ij} \boldsymbol{G}^i \otimes \boldsymbol{G}^j, \tag{31}$$

and

$$\boldsymbol{g} := g_{ij} \boldsymbol{g}^i \otimes \boldsymbol{g}^j, \tag{32}$$

respectively.

The displacement vector for a 3D continuum is defined as

$$\boldsymbol{u} = \boldsymbol{x} - \boldsymbol{R}, \tag{33}$$

where R is a position vector of point in the reference space.

The covariant components of the metric tensor in initial configuration are calculated as

$$G_{ij} = \boldsymbol{G}_i \cdot \boldsymbol{G}_j, \tag{34}$$

and the covariant components of a metric tensor in the deformed as

$$g_{ij} = \boldsymbol{g}_i \cdot \boldsymbol{g}_j. \tag{35}$$

The covariant basis vectors in the initial configuration are calculated with the first derivative of the position vector $\boldsymbol{R}$,

$$\boldsymbol{G}_i = \boldsymbol{R}_{,i}, \tag{36}$$

while the covariant basis vectors in the deformed configuration are calculated with the first derivative of the sum of the position vector in the initial configuration and the displacement vector, see Eq. (33)

$$\boldsymbol{g}_i = (\boldsymbol{R} + \boldsymbol{u})_{,i}. \tag{37}$$

2.4. Formulation of 3D finite elements

The derivation of a 3D finite element is described in this section. This finite element is used in numerical examples for modeling of the thick, soft substrate onto which the shell is attached. The derived 3D finite element has 8 nodes and at each node 3 degrees of freedom in terms of displacements. The element formulation is upgraded with the theory of incompatible modes to make it less stiff.

2.4.1. Interpolation of initial geometry of the 3D finite element

The geometry of the 3D finite element is interpolated with three linear Lagrange interpolation functions

$$N_I(\xi, \eta, \zeta) = \frac{1}{8}\{1 + \xi\xi_I, 1 + \eta\eta_I, 1 + \zeta\zeta_I\}, \tag{38}$$

where $\xi_I = \{-1, 1, 1, -1, -1, 1, 1, -1\}$, $\eta_I = \{-1, -1, 1, 1, -1, -1, 1, 1\}$ and $\zeta_I = \{-1, -1, -1, -1, 1, 1, 1, 1\}$. The interpolation of geometry is written as

$$\boldsymbol{R} = \sum_{I=1}^{8} N_I \boldsymbol{R}_I, \tag{39}$$

where the node position vectors $\boldsymbol{R}_I$ at the Ith node are written in a global basis $\{\boldsymbol{E}_1, \boldsymbol{E}_2, \boldsymbol{E}_3\}$ as

$$\boldsymbol{R}_I = R_{1_I} \boldsymbol{E}_1 + R_{2_I} \boldsymbol{E}_2 + R_{3_I} \boldsymbol{E}_3. \tag{40}$$

2.4.2. Compatible displacements

The classic approach is used for compatible displacement field interpolation where three linear interpolation functions from Eq. (38) are used

$$\boldsymbol{u} = \sum_{I=1}^{8} N_I \boldsymbol{u}_I. \tag{41}$$

The displacements at the Ith node are written in a global basis $\{\boldsymbol{E}_1, \boldsymbol{E}_2, \boldsymbol{E}_3\}$,

$$\boldsymbol{u}_I = u_{1_I} \boldsymbol{E}_1 + u_{2_I} \boldsymbol{E}_2 + u_{3_I} \boldsymbol{E}_3. \tag{42}$$

To determine the deformation gradient as defined in Eq. (4), it is first necessary to compute the displacement gradient, $\nabla \boldsymbol{u}$, given by

$$\nabla \boldsymbol{u} = \boldsymbol{u} \otimes \nabla = \frac{\partial u_i}{\partial R_j} \boldsymbol{E}_i \otimes \boldsymbol{E}_j. \tag{43}$$

Since $\boldsymbol{u}$ in Eq. (41) does not depend on R_j, $\nabla \boldsymbol{u}$ cannot be calculated directly. Therefore, the displacement gradient has to be calculated with the help of the chain rule

$$\frac{\partial u_i}{\partial R_j} = \frac{\partial u_i}{\partial \xi^k} \frac{\partial \xi^k}{\partial R_j}, \tag{44}$$

where $\xi^1 = \xi, \xi^2 = \eta$ and $\xi^3 = \zeta$. Expressions $\partial u_i / \partial \xi^k$ can be calculated directly from the interpolation of displacements in Eq. (41). Expressions $\partial \xi^k / \partial R_j$ represent the components of the Jacobian matrix, which is defined as

$$(\boldsymbol{J}) = \begin{pmatrix} \frac{\partial \xi}{\partial R_1} & \frac{\partial \xi}{\partial R_2} & \frac{\partial \xi}{\partial R_3} \\ \frac{\partial \eta}{\partial R_1} & \frac{\partial \eta}{\partial R_2} & \frac{\partial \eta}{\partial R_3} \\ \frac{\partial \zeta}{\partial R_1} & \frac{\partial \zeta}{\partial R_2} & \frac{\partial \zeta}{\partial R_3} \end{pmatrix}, \tag{45}$$

and its inverse as

$$(\boldsymbol{J}^{-1}) = \begin{pmatrix} \frac{\partial R_1}{\partial \xi} & \frac{\partial R_1}{\partial \eta} & \frac{\partial R_1}{\partial \zeta} \\ \frac{\partial R_2}{\partial \xi} & \frac{\partial R_2}{\partial \eta} & \frac{\partial R_2}{\partial \zeta} \\ \frac{\partial R_3}{\partial \xi} & \frac{\partial R_3}{\partial \eta} & \frac{\partial R_3}{\partial \zeta} \end{pmatrix}. \tag{46}$$

The covariant base vectors are defined as

$$\boldsymbol{G}_j = \frac{\partial \boldsymbol{R}}{\partial \xi^j} = \frac{\partial R_i}{\partial \xi^j} \boldsymbol{E}_i. \tag{47}$$

Multiplication of the covariant base vectors by $\boldsymbol{E}_k$ in Eq. (47) leads to

$$\boldsymbol{E}_k \cdot \boldsymbol{G}_j = \frac{\partial R_i}{\partial \xi^j} \boldsymbol{E}_k \cdot \boldsymbol{E}_i = \frac{\partial R_i}{\partial \xi^j} \delta_{ki} = \frac{\partial R_k}{\partial \xi^j}. \tag{48}$$

The expression in Eq. (48) represents components of the inverse Jacobian matrix,

$$(\boldsymbol{J}^{-1}) = \begin{pmatrix} \boldsymbol{E}_1 \cdot \boldsymbol{G}_1 & \boldsymbol{E}_1 \cdot \boldsymbol{G}_2 & \boldsymbol{E}_1 \cdot \boldsymbol{G}_3 \\ \boldsymbol{E}_2 \cdot \boldsymbol{G}_1 & \boldsymbol{E}_2 \cdot \boldsymbol{G}_2 & \boldsymbol{E}_2 \cdot \boldsymbol{G}_3 \\ \boldsymbol{E}_3 \cdot \boldsymbol{G}_1 & \boldsymbol{E}_3 \cdot \boldsymbol{G}_2 & \boldsymbol{E}_3 \cdot \boldsymbol{G}_3 \end{pmatrix}. \tag{49}$$

The Jacobian matrix is now

$$(\boldsymbol{J}) = \begin{pmatrix} \boldsymbol{E}_1 \cdot \boldsymbol{G}_1 & \boldsymbol{E}_2 \cdot \boldsymbol{G}_1 & \boldsymbol{E}_3 \cdot \boldsymbol{G}_1 \\ \boldsymbol{E}_1 \cdot \boldsymbol{G}_2 & \boldsymbol{E}_2 \cdot \boldsymbol{G}_2 & \boldsymbol{E}_3 \cdot \boldsymbol{G}_2 \\ \boldsymbol{E}_1 \cdot \boldsymbol{G}_3 & \boldsymbol{E}_2 \cdot \boldsymbol{G}_3 & \boldsymbol{E}_3 \cdot \boldsymbol{G}_3 \end{pmatrix}^{-T}. \tag{50}$$

Now all the components from the Jacobian matrix are derived and the displacement gradient $\nabla \boldsymbol{u}$ in Eq. (43) can be calculated.

2.4.3. Incompatible modes

In Ref. [45] the theory of incompatible modes is described in detail. With the help of this theory the formulation for 3D finite elements is derived. The entire formulation is based on the separation of displacement gradient into the compatible and incompatible parts. Such formulation of the displacement gradient is then used in the deformation gradient.

The displacement gradient is first divided into the compatible $\nabla \boldsymbol{u}$ and incompatible $\tilde{\boldsymbol{D}}$ parts

$$\overline{\boldsymbol{D}} = \nabla \boldsymbol{u} + \tilde{\boldsymbol{D}}, \tag{51}$$

where $\tilde{\boldsymbol{D}}$ can be written as

$$\tilde{\boldsymbol{D}} = \tilde{\boldsymbol{u}} \otimes \nabla. \tag{52}$$

Note that in general, the deformation gradient can be written as in Eq. (4). Since the displacement gradient is now written in the extended form with Eq. (51), the deformation gradient changes shape as well. This new deformation gradient will be denoted as $\overline{\boldsymbol{F}}$ and can be written as

$$\overline{\boldsymbol{F}} = \boldsymbol{G} + \overline{\boldsymbol{D}} = \boldsymbol{G} + \nabla \boldsymbol{u} + \tilde{\boldsymbol{D}}. \tag{53}$$

The compatible part $\nabla \boldsymbol{u}$ is calculated normally from the interpolation of displacements as written in Section 2.4.2 and the incompatible part $\overline{\boldsymbol{D}}$ is calculated from the new interpolation functions.

2.4.4. Incompatible displacement field

The incompatible displacement field $\tilde{\boldsymbol{u}}$ is not directly interpolated. Instead the displacement gradient is interpolated with interpolation functions $M_i(\xi, \eta, \zeta)$, $i = \{1, 2, 3\}$, which are of the higher order than the interpolation functions with which compatible displacements are interpolated. The interpolation functions for interpolation of incompatible displacement gradient are

$$M_I(\xi, \eta, \zeta) = \{1 - \xi^2, 1 - \eta^2, 1 - \zeta^2\}. \tag{54}$$

The incompatible displacement gradient can be written as

$$\tilde{\boldsymbol{D}} = \sum_{I=1}^{n_{im}} \nabla M_I \otimes \boldsymbol{\alpha}_I, \tag{55}$$

where n_{im} is the number of condensed incompatible degrees of freedom of the finite element (9 in our case) and $\boldsymbol{\alpha}_I$ are the incompatible degrees of freedom of the element which are condensed. Because the interpolation (55) cannot describe a constant stress field over the element, such as in the patch test, additional adjustments to these interpolations are needed. To do that, a minimal convergence requirement is derived, which imposes that the average value of the enhanced displacement gradient is zero in each element

$$\int_{\Omega^e} \tilde{\boldsymbol{D}} dV^e = \boldsymbol{0}, \tag{56}$$

where Ω^e represents the volume of the finite element. The modified interpolation can be now written as

$$\tilde{\boldsymbol{D}} = \sum_{I=1}^{n_{im}} \nabla \hat{M}_I \otimes \boldsymbol{\alpha}_I, \tag{57}$$

where fixed interpolation functions are defined as

$$\nabla \hat{M}_I = \nabla M_I - \frac{1}{\Omega^e} \int_{\Omega^e} \nabla M_I dV^e. \tag{58}$$

If now Eq. (58) is inserted into Eq. (57) and integrate over the volume of the element Ω^e, the condition in Eq. (56) is satisfied. One can write

$$\int_{\Omega^e} \nabla \hat{M}_i dV^e = \boldsymbol{0}. \tag{59}$$

Now all the variables in the extended version of the deformation gradient $\overline{\boldsymbol{F}}$ are known and can substitute $\boldsymbol{F}$ for it in Eq. (12).

2.5. Potential energy of the 3D-Solid_neo finite element

The potential energy of the 3D element with incompatible modes can be written as

$$\Pi^e(\boldsymbol{u}, \overline{\boldsymbol{D}}, \boldsymbol{P}) = \int_{\Omega^e} \{W(\boldsymbol{G} + \overline{\boldsymbol{D}}) + \boldsymbol{P} : (\nabla \boldsymbol{u} - (\boldsymbol{G} + \overline{\boldsymbol{D}}))\} dV^e. \tag{60}$$

Because of Eq. (53), the above functional can be written as

$$W(\boldsymbol{G} + \overline{\boldsymbol{D}}) = W(\overline{\boldsymbol{F}}). \tag{61}$$

Since the formulation of the 3D element contains incompatible modes, the deformation gradient $\boldsymbol{F}$ in Eq. (12) can be replaced with $\overline{\boldsymbol{F}}$ with incompatible modes. The right Cauchy–Green deformation gradient with incompatible modes becomes

$$\boldsymbol{C} = \overline{\boldsymbol{F}}^T \overline{\boldsymbol{F}}. \tag{62}$$

If the Green–Lagrange deformation tensor is written as $\boldsymbol{E} = (\boldsymbol{C} - \boldsymbol{G})/2 = (\overline{\boldsymbol{F}}^T \overline{\boldsymbol{F}} - \boldsymbol{G})/2$, the tensor $\boldsymbol{C}$ can be also written as

$$\boldsymbol{C} = \overline{\boldsymbol{F}}^T \overline{\boldsymbol{F}} = 2\boldsymbol{E} + \boldsymbol{G}. \tag{63}$$

In our numerical simulations, the structures are subjected also to temperature load. Therefore, a related part has to be added to the Green–Lagrange deformation tensor

$$\boldsymbol{E} = \frac{1}{2}(\boldsymbol{C} - \boldsymbol{G}) + \alpha_t \boldsymbol{G} \bar{T}, \tag{64}$$

where α_t and $\bar{T}$ are the linear temperature expansion coefficient and change in temperature. It follows from Eqs. (63) and (64) that

$$\boldsymbol{C} = \overline{\boldsymbol{F}}^T \overline{\boldsymbol{F}} - 2\alpha_t \boldsymbol{G} \bar{T}. \tag{65}$$

Furthermore, based on Eq. (62), the strain energy density function of the neo-Hookean material model from Eq. (1) can be written as

$$W(\boldsymbol{C}) = W(\overline{\boldsymbol{F}}). \tag{66}$$

We name the finite element with the strain energy density function Eq. (66) in functional Eq. (60), 3D-Solid_neo.

The minimum potential energy of the 3D-Solid_neo finite element, is calculated with the first variation of Eq. (60)

$$\delta \Pi^e = \frac{d}{d\varepsilon} \left[\Pi^e(\boldsymbol{u} + \varepsilon \delta \boldsymbol{u}, \overline{\boldsymbol{D}} + \varepsilon \delta \overline{\boldsymbol{D}}, \boldsymbol{P} + \varepsilon \delta \boldsymbol{P}) \right] \Big|_{\varepsilon=0} = 0, \tag{67}$$

and more precisely

$$\delta \Pi^e(\boldsymbol{u}, \delta \boldsymbol{u}, \overline{\boldsymbol{D}}, \delta \overline{\boldsymbol{D}}, \boldsymbol{P}, \delta \boldsymbol{P}) = \int_{\Omega^e} \left\{ \boldsymbol{P} : \nabla \delta \boldsymbol{u} + \left(\frac{\partial W}{\partial \overline{\boldsymbol{F}}} - \boldsymbol{P} \right) : \delta \overline{\boldsymbol{D}} + \right. \\ \left. + (\nabla \boldsymbol{u} - \overline{\boldsymbol{D}}) : \delta \boldsymbol{P} \right\} dV^e. \tag{68}$$

Eq. (68) presents a weak form of the 3D-Solid_neo finite element. The volume integrals in this expression are calculated with a classical $2 \times 2 \times 2$ Gaussian integration rule.

3. Numerical simulations and experiments

In order to solve the system of equations by an incremental-iterative Newton–Raphson procedure (which is a part of the applied path-following method), the equations have to be consistently linearized. However, it should be noted that variation and linearization were performed using Mathematica [48] and its add-on AceGen [49]. The

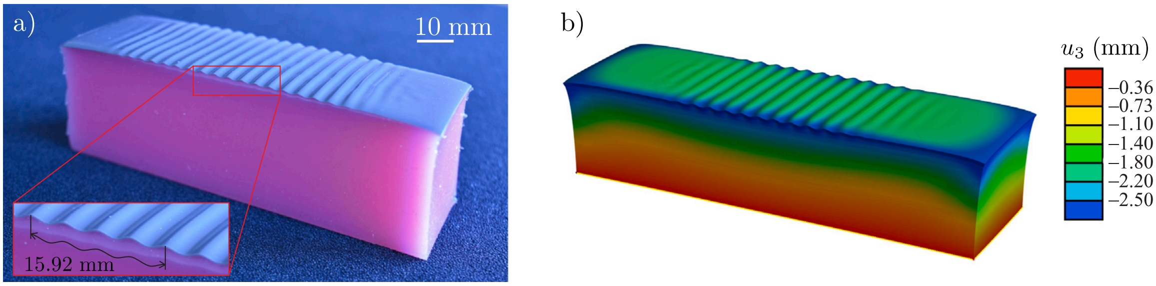

Fig. 1. Uniaxial wrinkling of a rectangular plate on a soft substrate. (a) Experiment, (b) Numerical simulation. Geometric properties of the plate (gray part) were: thickness $h = 0.22$ mm, length $L = 102.0$ mm, width $w = 30.0$ mm, while the thickness of the substrate (pink part) was $H = 25.0$ mm. Young's moduli and Poisson ratios of the film and the substrate were: $E_f = 4.27$ MPa, $E_s = 0.072$ MPa and $\nu = \nu_f = \nu_s \doteq 0.49$. An average wavelength obtained in the experiment was $\lambda_{\text{exp}} = 3.98$ mm (see the inset in panel a), while in simulation $\lambda_{\text{num}} = 4.02$ mm was obtained. The color scale represents displacements u_3 in the normal direction to the plate surface.

derived finite elements were implemented in the AceFEM [49] computer code. To solve the nonlinear system of equations, fairly robust arc-length procedures described in [50–52] were used.

Four experiments in which wrinkling was observed on plates and shells attached to thick substrates were performed. The (rectangular and circular) plates and (cylindrical and hemispherical) shells were essentially thin films made from polymer QSil 550 (gray color), which had a higher modulus of elasticity than the substrate made from the softer polymer Zhermack Elite Double 8 (pink color). Both polymers were initially liquid and then changed to a solid phase. Exactly 50 % by mass of a silicone oil was added to the substrate material, which served as a softener to (i) reduce its Young's modulus and thus increase the ratio between Young's moduli of both materials and to (ii) pronounce its shrinkage during solidification, resulting in compression in the plates and shells. Both polymers were firmly bonded together at the contact surface when the substrate material was poured onto the already solidified plates and shells. Moreover, no slip or delamination between the two materials was observed during the experiments within the prescribed constraints. Further details on the fabrication procedure are given in Appendix A. The material properties of the films and the soft substrates were determined from the bending, compression and volumetric tests, see Appendix B.

The substrate shrinkage was modeled by analogy – through cooling – and maintaining a constant temperature within the plates and shells throughout the analysis. This mirrored the experimental conditions where the shell was completely solidified before coming into contact with the initially liquid substrate (see Appendix A). Since the temperature difference was used in the analysis, we had to assign an appropriate value for the coefficient of thermal expansion for silicone materials $\alpha_T = 9 \cdot 10^{-6}$ K^{-1}, which was taken from the literature. The value of α_T had no influence on the shape of the deformation pattern; it only affected the magnitude of the temperature change required to induce wrinkling. As the temperature expansion coefficient was very small, the temperature difference required in the analysis was very high, and took values up to −4000 K, which is, of course, non-physical and has only numerical significance. Alternatively, one could also opt for the use of artificially larger α_T instead.

3.1. Uniaxial wrinkling of a rectangular plate

Fig. 1(a) shows the uniaxial wrinkling on a rectangular plate caused by the shrinkage of the substrate. It is important to note that although the compressive stresses in the substrate are generally spatial, they are significantly larger in the longitudinal direction of the structure. As a result, and due to the free boundary conditions, wrinkling is predominantly uniaxial and occurs first around the mid-length of the plate. Therefore, wrinkles with larger amplitudes are found there, while they gradually decrease towards the two ends along the length.

The average wavelength measured along the arc-length of the waves was $\lambda_{\text{exp}} \doteq 3.98$ mm. As the materials used are practically incompressible (see Appendix B), the arc-length of the deformed configuration is practically the same as that of the undeformed configuration. The results can thus be compared directly to the theoretical wavelength $\lambda_{\text{th}} = 3.74$ mm, which is calculated from Eq. (20b) in [53]. A fairly good agreement with a relative difference of 6.1% is obtained.

In numerical simulations, 9733 DKQ-5_neo shell finite elements and 116,796 3D-Solid_neo solid finite elements were used to model the response of the plate and the substrate, respectively. The nodes at the bottom of the plate were restricted to move only in-plane and a few points there (at the mid-length) were fixed to prevent rigid body motion. The material and geometric properties were the same as in the experiment, see caption of Fig. 1. The numerically determined deformed configuration in Fig. 1(b) shows excellent qualitative agreement with the experiment, as here too the first wrinkles appeared in the middle of the surface of the plate (where they are also more pronounced later) and gradually fade away towards both ends. Excellent agreement is also achieved quantitatively, since an average wavelength of $\lambda_{\text{num}} = 4.02$ mm obtained in the simulations differs only by 1.0% from the experiments.

3.2. Uniaxial (circumferential) wrinkling of a cylindrical shell

The second experiment to validate the developed computational model was made on a cylindrical shell, which, unlike the first experiment, has curvature in one direction. The same procedure was followed in fabrication of this test specimen as for the uniaxial wrinkling experiment. Once the plate was solidified and demolded, it was carefully placed on the inner surface of a cylindrical mold. Due to this fabrication process, the cylindrical shell was not continuous in the circumferential direction and had a small imperfection where the two edges met when it was placed in the mold. Next, a pink liquid silicone/silicone oil mixture was poured into the cylindrical mold and allowed it to solidify. Again, a tight adhesion formed between the shell and the substrate. More details on the fabrication procedure are given in Appendix A. As the substrate material solidified and shrank, compressive stresses developed within the shell material, ultimately leading to wrinkling.

Fig. 2(a) shows the deformed shape of the cylindrical shell on a substrate. The wrinkles have formed uniformly around the circumference of the shell and are aligned parallel to the cylinder's longitudinal axis. This pattern is qualitatively similar to the uniaxial wrinkling experiment, but now curved along the principal curvature. The average wavelength measured in this experiment was $\lambda_{\text{exp}} \approx 5.68$ mm while the theoretical prediction yielded $\lambda_{\text{th}} = 5.27$ mm, resulting in a relative difference of 7.3%.

In the experiment, the cylinder was completely filled with the substrate material. However, in the numerical analysis that followed, the inside of the substrate was made hollow to reduce the number of

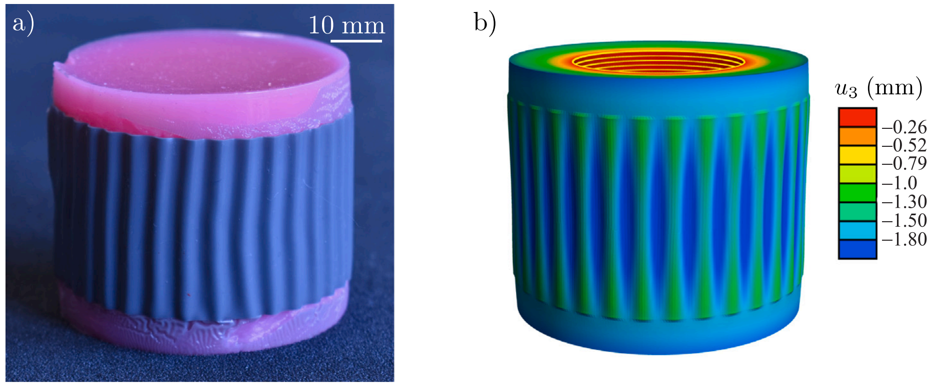

Fig. 2. Uniaxial (circumferential) wrinkling of a cylindrical shell. (a) Experiment, (b) Numerical simulation. Geometric properties of the shell (gray part) were: outer diameter $D = 59.3$ mm, thickness $h = 0.1$ mm, width (height) $H_f = 35.0$ mm, while width (height) of the substrate (pink part) was $H_s = 50.7$ mm. The material properties were the same as before. Note that unlike the experimental sample, the sample in the numerical simulation has a hole with diameter $d = 32$ mm in the center. An average wavelength obtained in the experiment was $\lambda_{\text{exp}} = 5.68$ mm, while in simulation $\lambda_{\text{num}} = 5.645$ mm was obtained. The color scale represents displacements u_3 in the radial direction.

3D solid finite elements used and decrease the computational time. Note that despite being hollow, the substrate remained sufficiently thick to promote localized deformation. The numerical analysis was conducted using 31,097 of our DKQ-5_neo elements and 443,244 3D-Solid_neo finite elements. All nodes on the inner surface of the substrate were prevented from moving in the radial direction. In addition, nodes located on a circle at the mid-height of the cylinder were also prevented from moving in the vertical and tangential directions.

From the deformed shape depicted in Fig. 2(b), the wavelength along the circumference of the cylinder was evaluated, again measured along the arc length of the deformed configuration of the shell. Our analysis yielded an average wavelength of $\lambda_{\text{num}} = 5.645$ mm. When quantitatively comparing the numerically determined wavelength with the one observed in the experiments, a very good match with a relative difference of only 0.62% was found. However, unlike in the experiments we observed that the amplitude of wrinkles was greater at the mid-height of the shell and diminished towards the edges in numerical simulations. We attribute this to the fixed boundary conditions at the mid-height of the cylinder that were imposed to prevent rigid body motion.

3.3. Wrinkling on a circular plate

Similarly to the first two experiments, again the (circular) plate was made first. Once the plate had solidified, it was placed in another cylindrically shaped mold. The plate was positioned on the circular face of the mold and the pink polymer/oil mixture was poured over it to fabricate the substrate which adhered to the plate in the process. The sample was left in the mold to minimize its bending that would otherwise occur during solidification because of the non-symmetric composition (through-the-thickness) of the whole system (the plate is only on one side). Because the plate was kept the mold, the diameter of the cylindrical mold had to be larger than that of the circular plate to reduce the effects of the edge that prevented the plate from freely deforming during shrinking of the substrate. In this case, the shrinkage during solidification of the substrate material induced an (approximately) homogeneous in-plane deformation field (far enough from the edge) that led to the formation of a corresponding wrinkling pattern in the form of a zigzag/labyrinthine pattern, as depicted in Fig. 3(a).

To determine the average wavelength between neighboring channels, we had to identify some nodes at the peaks of the wrinkles on the deformed configuration first and measure the distances between these nodes by mapping them into the initial configuration. The measured wavelength of the experimentally obtained wrinkling pattern was $\lambda_{\text{exp}} \approx 4.82$ mm, while the theoretical prediction yielded $\lambda_{\text{th}} = 4.59$ mm. The relative difference between both results was therefore 4.8%.

For the numerical analysis, we again used DKQ-5_neo and 3D-Solid_neo finite elements. The plate mesh comprised 10,169 elements and the substrate mesh 141,468 elements. All vertical displacements on the bottom face of the substrate were disabled in the simulations as in the 1D flat case. To prevent rigid translation of the entire model, a small region of nodes in radius of 3 mm around the vertical axis of the cylinder at the bottom of the substrate was disabled to move also horizontally. It has to be noted that the boundary conditions in this case were again not an exact match to the ones in experiment, but yielded the most similar results. At the onset of wrinkling instability in the experiments, the wrinkles emerged across the entire plate almost simultaneously, while in numerical simulations they emerged first in the center of the plate and gradually spread towards the edge of the plate. An average wavelength computed numerically was $\lambda_{\text{num}} = 4.786 \pm 0.194$ mm, which means that only a 0.70% difference was found compared to experiments.

It is important to point out that all three examples so far had zero Gaussian curvature in an undeformed configuration so that the localized/discretized units of deformation (i.e. wrinkles) had to interact only among themselves in all the obtained wrinkling patterns. In the next example, wrinkling on hemispheres will be examined, adding another dimension of complexity, as the pattern must also interact with the non-zero Gaussian curvature of the substrate.

3.4. Wrinkling of a hemispherical shell

The most interesting wrinkling case investigated in this paper using the developed computational model involved a hemispherical shell on a soft substrate. To create the hemispherical shell, a coating technique was employed, as reported in [54]. Specifically, liquid silicone was poured over a steel ball from a ball bearing. Once the liquid silicone fully solidified, the ball was carefully removed from the silicone enclosing the ball. Then the resulting shell was suspended upside down, supporting it at the edge that was created when the excess liquid polymer was drained from the shell due to gravity and gathered at the equator. Subsequently, the shell's interior was filled with the mix of the pink liquid polymer–silicone oil to create the substrate. More details on the fabrication procedure are given in Appendix A.

Upon solidification of the substrate material, subsequent shrinkage induced compression stresses within the shell. This phenomenon led to the formation of a wrinkling pattern comprising dimples radiating from the pole/apex towards the equator, as well as vertical channels at the equator (see Fig. 4). The presence of these channels can be attributed

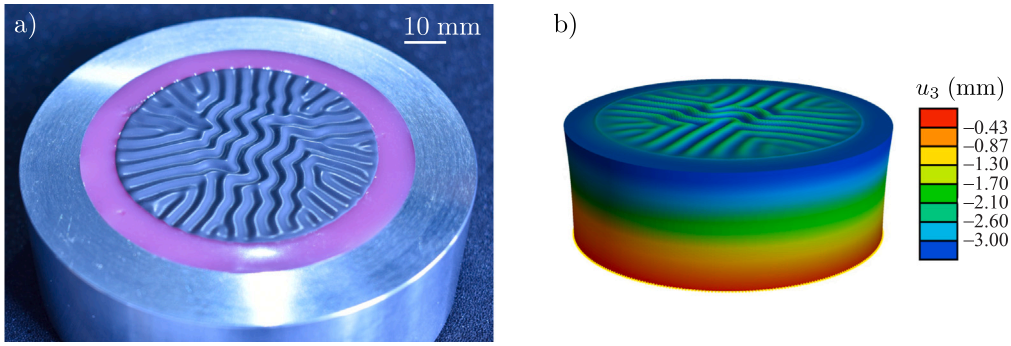

Fig. 3. Wrinkling of a circular plate. (a) Experiment, (b) Numerical simulation. Geometric properties of the plate (gray part) were: thickness $h = 0.27$ mm, diameter $D_f = 62.7$ mm, while the substrate (pink part) had thickness $H = 30.0$ mm and diameter $D_s = 80.0$ mm. The material properties were the same as in the previous two experiments. An average wavelength obtained in the experiment was $\lambda_{\text{exp}} = 4.82$ mm, while in simulation $\lambda_{\text{num}} = 4.786 \pm 0.194$ mm was obtained. The color scale represents displacements u_3 in the normal direction to the plate surface.

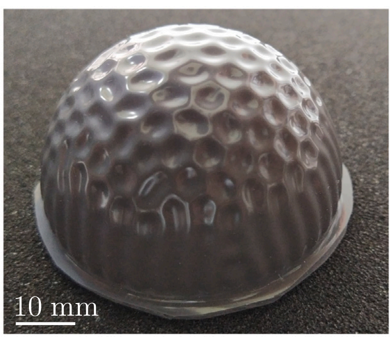

Fig. 4. Wrinkling experiment of a hemispherical shell. Geometric properties were as follows: inner shell diameter $D = 50.0$ mm, thickness $h = 0.27$ mm. The material properties were the same as in the previous experiments.

to a thin hoop that formed after the excess material accumulated there due to drainage and provided additional local rigidity in the hoop direction. In our case, the shrinkage of the substrate without it leads to delamination between the shell and the substrate that tends to propagate further towards the apex as the shrinkage is progressing.

Using the same procedure as in [55], the average wavelength of this pattern was measured using 3D scanning and the concept of a Voronoi diagram. The obtained value was $\lambda_{\text{exp}} \approx 5.13 \pm 0.41$ mm. Based on the established geometric and material properties of the shell/substrate composite the theoretical wavelength was determined $\lambda_{\text{th}} = 4.59$ mm. This corresponds to a relative difference of 10.6% when compared to experimental observations.

To attest the proposed computational model also on a shell of non-zero Gaussian curvature, ten different numerical analyses of a hemisphere with different combinations of boundary conditions were performed. As it turns out, the aforementioned hoop at the equator and the fact that shrinkage at the equator is thus constrained, make it even more difficult to determine the boundary conditions. The illustrations of the boundary conditions, deformed shapes and geometrical properties with the results are shown in two sets of five samples in Figs. 5 and 6 in separate columns.

In example A, the shell was modeled using the developed DKQ-5_neo shell finite element, while the substrate was modeled as a Winkler type foundation with coefficient of stiffness $K_s = 0.0580$ N/mm^3. The shell was subjected to surface pressure p. This example is also the only one where the Winkler's foundation was used instead of the solid substrate and the surface pressure was used as an external load. In all other cases, the substrate was modeled using our 3D-Solid_neo finite elements and the analogy of cooling the substrate was applied to induce the compression stresses in the shell.

With increasing external pressure load p, or equivalently decreasing the temperature T in the substrate, the dimple pattern initially appeared on the top of the hemisphere and later spread towards the edge of the hemisphere. From a quick comparison of the deformation shapes provided in the second column of Figs. 5 and 6 one can observe that the results are not the same in all the analyzed examples. It was noticed that the deformation patterns strongly depend on the boundary conditions. In example A, the dimples appeared over the entire shell surface, including near the edge (at the equator). A similar deformation pattern was observed in example C. In example B, where the bottom edge displacements and rotations were not disabled, the wrinkle pattern exhibits vertical parallel grooves. Grooves can also be seen in examples I and J in Fig. 6, although slightly away from the edge of the shell due to the fixed displacements and rotations there. We noticed an interesting phenomenon in the analyses, where displacements at the bottom surface of the substrate were fixed. In examples D–F, a horizontal channel appeared parallel to the equator, such that the shell's edge resembles an elephant's foot. It is a phenomenon otherwise characteristic for an elasto-plastic buckling of thicker axisymmetric shells (see e.g. [56]) . In all these analyses all displacements were disabled at the edge or at least displacements in the vertical direction at the bottom of the substrate. Furthermore, also rotations at the edge of the hemisphere in sample B were disabled. In examples A–H the interior of the hemisphere was not completely filled with the substrate, while in cases I and J it was. As expected, comparison of the results from examples G and I, where the boundary conditions were the same, but G had a cavern in the substrate, revealed that the average wavelengths are practically the same. Surprisingly, the coverage with dimples is not. example G is only partially covered with dimples (emanating from the apex/pole), while example I exhibits the aforementioned parallel vertical channels at the equator.

In those analyses where the dimple pattern appeared over the majority of the shell's surface we noticed that the distances between the dimples at the top of the hemisphere were smaller than those closer to the edge of the hemisphere. Therefore, in some analyses the distances between the dimples were calculatedcloser to the top of the hemisphere and separately also for the entire surface of the hemisphere. In Figs. 5 and 6 we labeled with α the polar angle that defines an area around the polar cap that we used to calculate the average wavelength between the dimples. From the calculated average wavelengths between the neighboring dimples it was found out that the results obtained in examples H and J are the closest to the experimental data in Section 3.4. In these two analyses, the thickness of the shell was not modeled as constant, but varied it linearly with the polar angle α from the top towards the bottom of the hemisphere. At the top of the

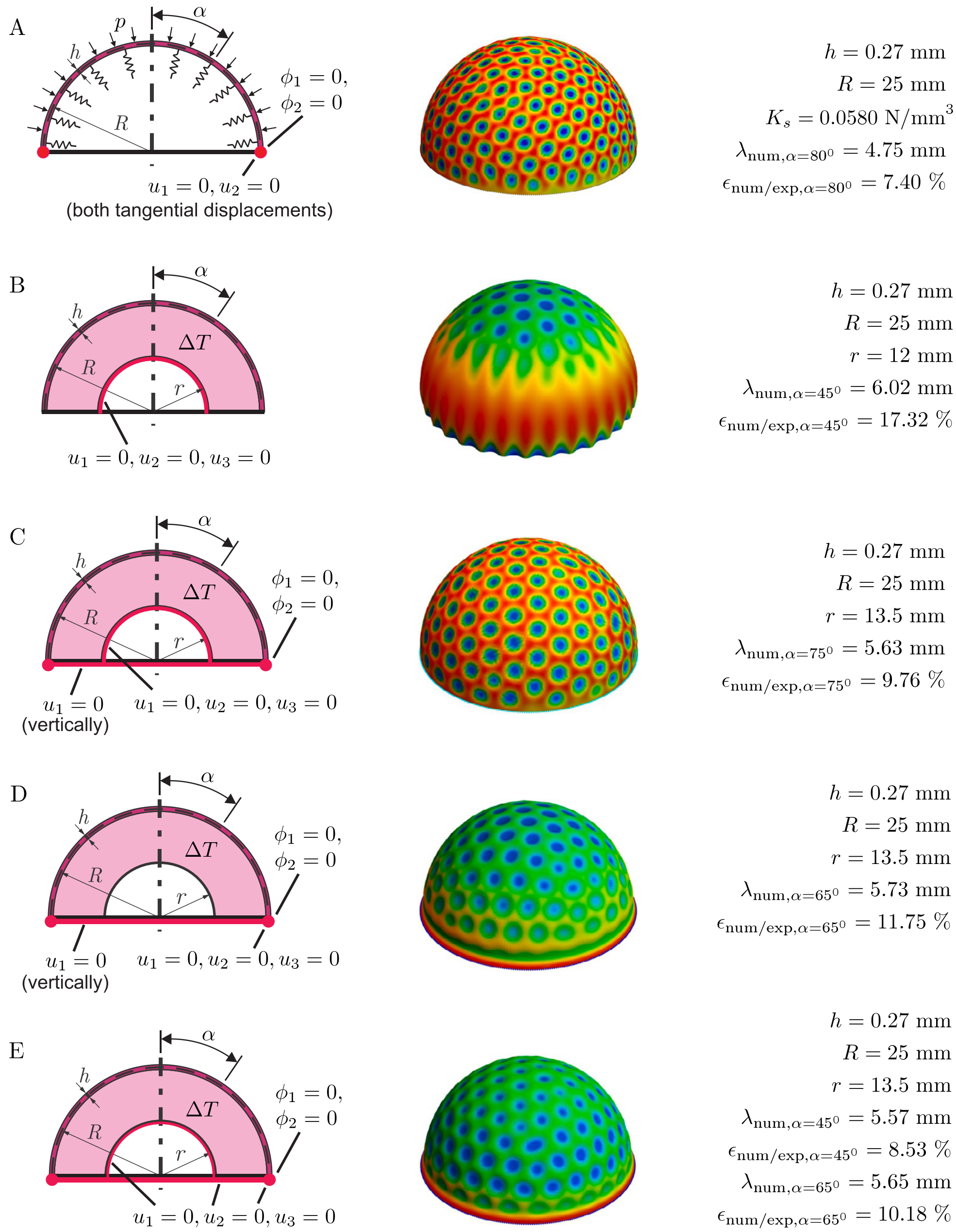

Fig. 5. The first set of five numerical simulations of wrinkling of a hemisphere. Each column represents illustrations with boundary conditions, deformed shapes and geometrical properties with results. The colors on the deformed shapes (used only for visual comparison) represent the intensity of radial displacements u_3.

hemisphere the thickness was made slightly smaller than at the bottom, as observed in the experiment. The variation ranged from 0.25 mm to 0.29 mm. The results of the numerical analysis of example H showed that the average wavelength between the dimples up to $\alpha = 45°$ was $\lambda_{\text{num},\alpha=45°} = 5.45$ mm, which gives $\epsilon_{\text{num/exp},\alpha=45°} = 6.17\%$ of relative difference between the numerical and the experimental value $\lambda_{\text{exp}} = 5.13$ mm. In example J, the average wavelength between the dimples was $\lambda_{\text{num},\alpha=40°} = 5.54$ mm at $\alpha = 40°$, which gives $\epsilon_{\text{num/exp},\alpha=40°} = 8.0\%$ of relative difference compared to the experimental value. It can be observed that the calculated wavelength in case H is slightly closer to the experimental value. Based on the deformation shape one can see that in the vicinity of the edge the wavy deformation shape was not formed as in the experiment. In example J, the deformation shape was almost the same as the deformation shape obtained in the experiment (see Fig. 4). In all other analyses, the average wavelengths between the dimples differ more significantly from the experimental value.

The results are summarized in Table 1 where all the experimental, corresponding numerical and theoretical results are gathered. It can be noted that the results from the experiments and simulations match quite well with the exception of the results for the hemisphere wrinkling, where boundary conditions were difficult to determine to match those in the experiments.

4. Conclusion

In this paper, we presented a new computational tool for accurate simulation of wrinkling instability observed in thin plates and shells on soft shrinking substrates. This tool will enable more rigorous studies

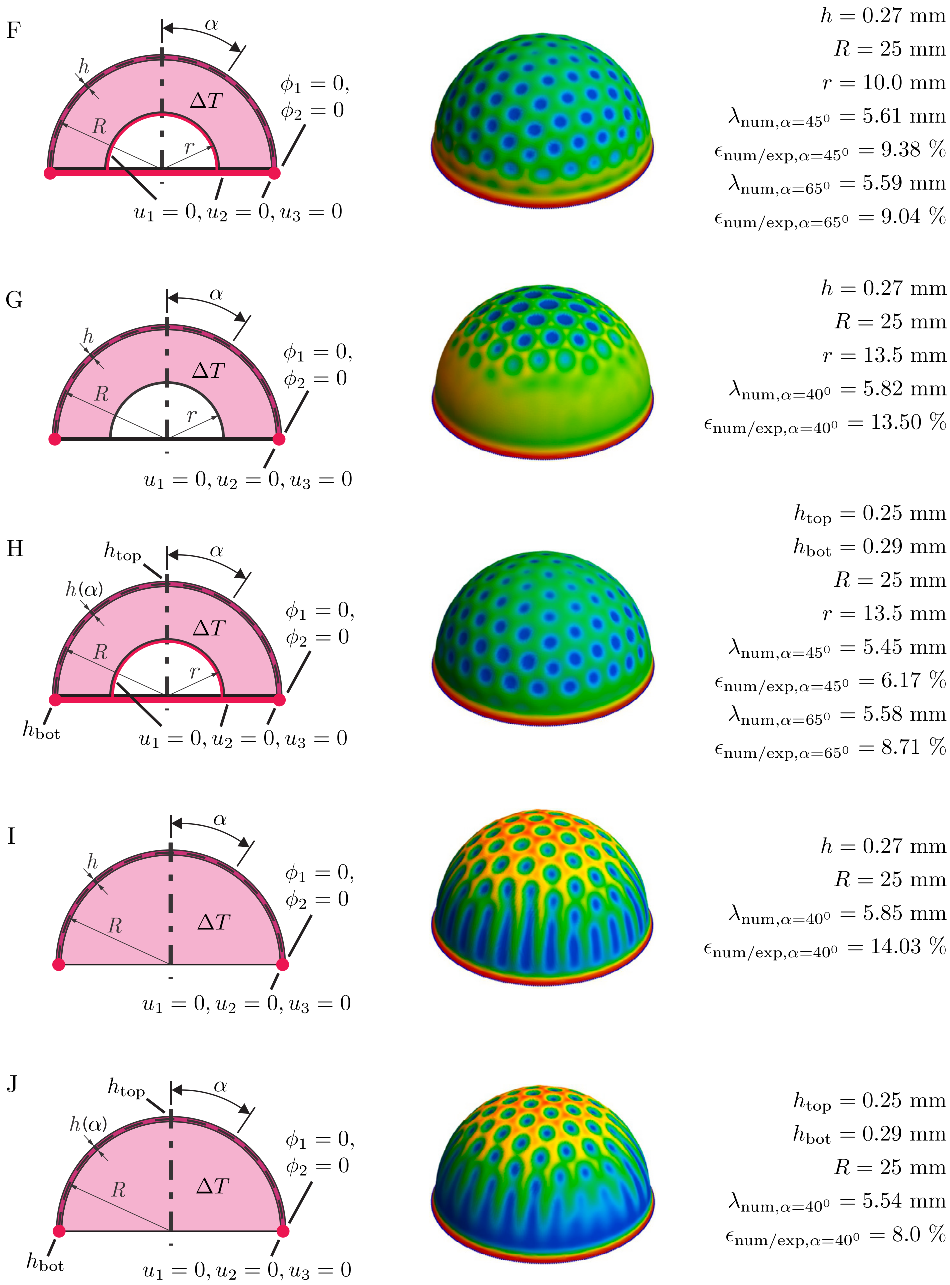

Fig. 6. The second set of five numerical simulations of wrinkling of a hemisphere. Each column represents illustrations with boundary conditions, deformed shapes and geometrical properties with results. The colors on the deformed shapes (used only for visual comparison) represent the intensity of radial displacement u_3.

Table 1
Summary of the results.

Example	λ_{exp} (mm)	λ_{num} (mm)	λ_{th} (mm)	$\epsilon_{\mathrm{num/exp}}$ (%)	$\epsilon_{\mathrm{th/exp}}$ (%)
Uniaxial	3.98	4.0	3.74	1.0	6.1
Cylindrical	5.68	5.64	5.27	0.62	7.3
Circular	4.82	4.79 ± 0.19	4.59	0.70	4.8
Spherical	5.13 ± 0.41	5.45–6.02	4.59	6.17–17.32	10.6

and the development of various applications mentioned in the introduction, as well as insight into the fundamental physics of the process. Furthermore, it was demonstrated that experimental validation of such simulations can be achieved through comparatively simple fabrication procedures of physical samples, which is crucial as it provides a “reality check” for any theoretical or numerical investigation.

More specifically, we simulated wrinkling of thin plates and shells with Kirchhoff–Love shell finite elements developed in [29] and the substrates with 3D hexahedral 8 node finite elements, whose formulation we derived from the theory of incompatible modes. Compressive stresses were imposed on the structures through cooling of the substrates, which mimicked shrinking during the solidification of the PDMS polymer in the experiments. It was noticed that the otherwise natural shrinking of this during solidification can be pronounced and controlled by the addition of a silicone oil. A neo-Hookean material model was implemented instead of St. Venant-Kirchhoff’s to obtain a more accurate description of material behavior in compression at larger strains. The deformation patterns in numerical analyses were

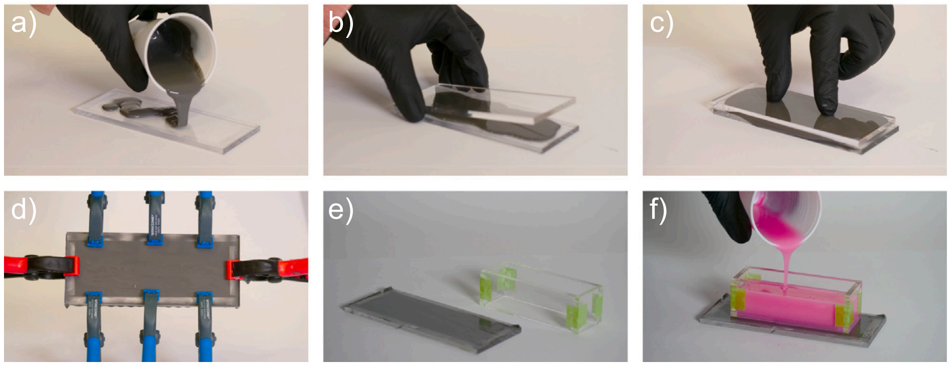

Fig. A.1. Fabrication procedure of the rectangular plate on a substrate. (a) Liquid polymer QSil 550 (gray color) was poured into a thin frame/mold that was made from an acrylic foil and attached to an acrylic plate. The thickness of the frame determined the thickness of the plate. (b) To achieve a uniform thickness another acrylic plate was carefully placed over the liquid polymer to squeeze out the access polymer by (c) pressing it against the frame. (d) Clamps were attached to the frame so that the film can solidify. (a) After approximately 48 h the top plate was removed and another frame/mold with a height that determined the substrate thickness was placed over the film. In the final step (f) a liquid polymer Zhermack Elite Double 8 (pink color) with the addition of a silicone oil 50% by mass was poured into the frame/mold. After approximately 1 h the sample was freed from all the constraints to shrink freely.

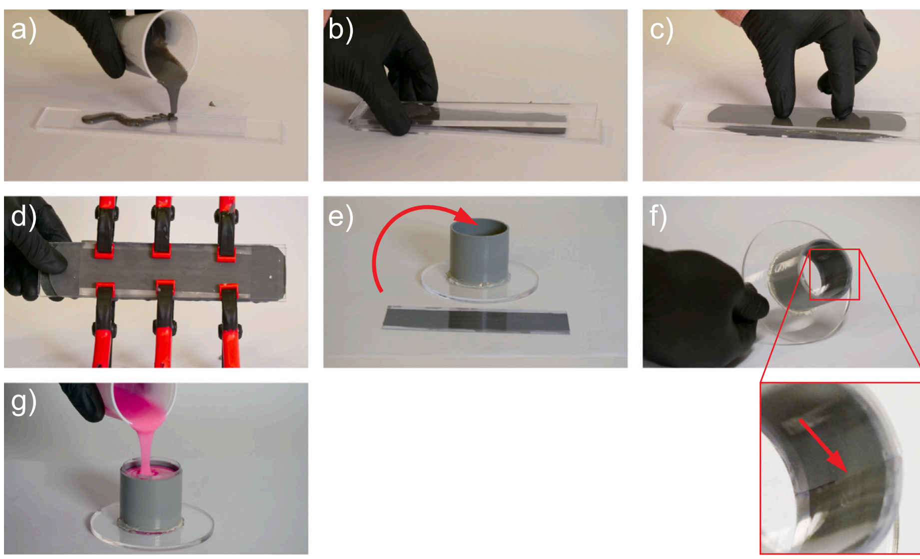

Fig. A.2. Fabrication procedure of the cylindrical shell on a substrate. Steps (a)-(d) are exactly the same as described in the caption of Fig. A.1. The only, and key, difference is that the thin acrylic frame is attached onto another acrylic foil that is (e) removed from the clamps and cut to a length that corresponds to the circumference of the cylindrical mold (light gray color). After approximately 48 h (f) the thin acrylic foil with the solidified silicone film is bent into a cylindrical shape and placed inside the mold. The inset on the bottom shows an imperfect seam where the two ends of the film meet. (g) A liquid polymer Zhermack Elite Double 8 (pink color) with the addition of a silicone oil 50% by mass was poured into the frame/mold. After approximately 1 h the sample was freed from all the constraints to shrink freely.

very similar to the deformation patterns observed in experiments. A good agreement between the calculated wavelengths of the neighboring wrinkles from numerical simulations, experiments and theoretical predictions confirmed the predictive power of the proposed numerical procedure.

CRediT authorship contribution statement

Tomo Veldin: Writing – original draft, Software, Methodology, Investigation, Formal analysis, Conceptualization. **Jonas Trojer:** Writing – review & editing, Visualization, Methodology, Formal analysis, Conceptualization. **Boštjan Brank:** Writing – review & editing, Supervision, Software, Methodology, Investigation, Formal analysis, Conceptualization. **Miha Brojan:** Writing – review & editing, Visualization, Validation, Resources, Project administration, Methodology, Investigation, Formal analysis, Conceptualization.

Declaration of competing interest

The authors declare that they have no known competing financial interests or personal relationships that could have appeared to influence the work reported in this paper.

Acknowledgment

Authors J.T. and M.B. gratefully acknowledge the financial support of the Slovenian Research Agency (project grant numbers J2-9223 and J2-2499).

Appendix A. Fabrication procedure of the plate and shell structures

Fabrication procedures of all the samples are depicted in Figs. A.1–A.4 with details given in their captions.

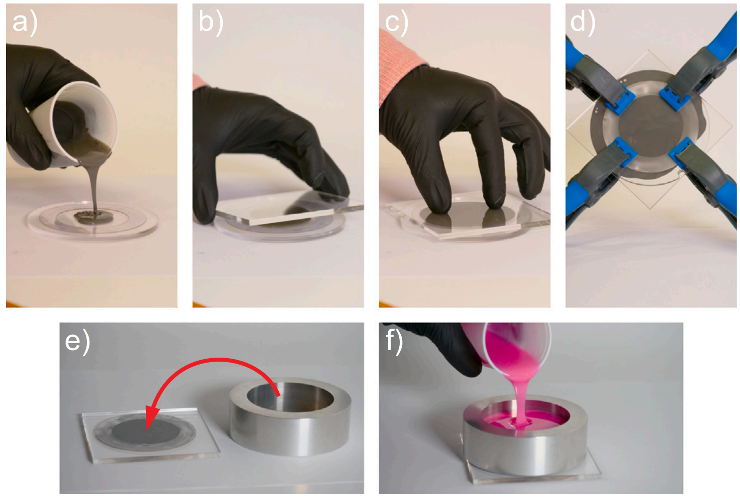

Fig. A.3. Fabrication procedure of the circular plate on a substrate is exactly the same as described in the caption of Fig. A.1.

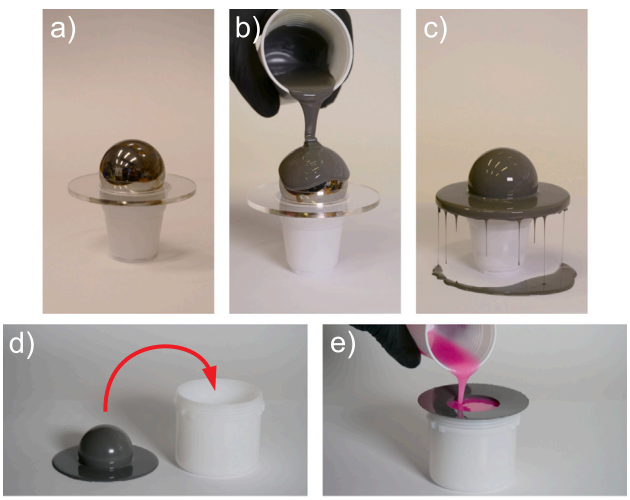

Fig. A.4. Fabrication procedure of a hemisphere on a substrate. (a) A steel ball is placed at the center of an acrylic annulus that rests on a cup. (b) Liquid polymer QSil 550 (gray color) was poured over the steel ball to make the hemispherical shell. (c) Excess polymer dripping from the edge of the annulus. (d) After approximately 48 h an aggregate of a solidified polymeric annulus and a hemisphere was turned upside down and placed over a cup. In the final step (e) a liquid polymer Zhermack Elite Double 8 (pink color) with the addition of a silicone oil 50% by mass was poured into the hemisphere. After approximately 1 h the sample was freed from all the constraints to shrink freely.

Appendix B. Material testing

Bending, compression and volumetric tests were conducted to determine the material constants needed in our simulations. These were Young's moduli of the film and the substrate E_f and E_s, respectively, and the corresponding volumetric tests to determine the Poisson's ratios ν_f and ν_s.

B.1. Bending tests to evaluate E_f

Bending is the predominant deformation mode in the thin plates and shells that were used in the wrinkling experiments. Therefore, the goal was to determine the Young's modulus E_f with bending tests. We analyzed large displacements of three cantilever beams with the same cross section, different lengths and made from silicone polymer QSil 550 – the same as the plates and shells. The beams were subjected only to gravity. Fig. B.1 shows deformed shapes of the three beams, together with numerically calculated deformed middle surface lines. The deformed middle surface lines were calculated with the DKQ-5_neo finite element by iteratively changing Young's modulus of the material to get the best fit to the experiments.

The beams had the following geometric properties: length $L = \{139.9, 109.9, 80.5\}$ mm, width $w = 19.95$ mm, thickness $h = 3.15$ mm. Based on the snapshots of the displacement curve the Young's modulus of the thin layer material was determined. The best agreement between middle surface lines and experiments was observed with the value of Young's modulus of $E_f = 4.27$ MPa. In the numerical analysis, equivalent surface load instead of the weight of the beams was used. The load was chosen based on the density of material, height of the beam and gravitational acceleration $p = g\rho h$, where the density of the polymer was $\rho = 2004 \cdot 10^{-9}$ kg/mm^3.

B.2. Compressive test to evaluate E_s

The Young's modulus of the substrate E_s was evaluated with a compression test on a Zwick/Roell Z050 universal testing machine. A cylindrically shaped specimen made from Zhermack Elite Double 8 polymer with diameter $d = 29.0$ mm and height $h = 12.5$ mm was placed between two rigid plates, as shown in Fig. B.2(a). In the experiment the reaction force F and the displacement Δh were measured continuously. The plot in Fig. B.2(b) shows that a linear fit with the experimental curve makes an excellent approximation.

B.3. Volumetric tests to evaluate ν_f and ν_s

The Poisson's ratios of the plate/shell and the substrate material, ν_f and ν_s, respectively, were determined with the volumetric test. Two cylindrical samples made from each material with diameter of $d = 10.0$ mm and height $h = 20.0$ mm were inserted into a bore that was made through the center of a steel cylinder and compressed with a steel piston with a slightly smaller diameter, as shown in Fig. B.3(a). Once more, a linear fit was employed to approximate the measurement results, as illustrated in the diagrams in Fig. B.3(b), depicting the applied force F relative to vertical displacement Δh.

Data availability

Data will be made available on request.

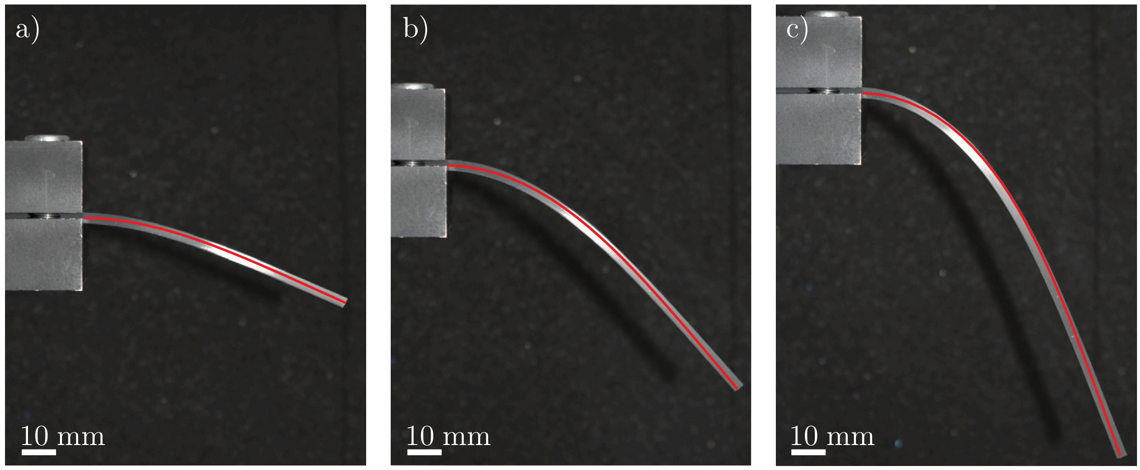

Fig. B.1. Bending test on beams subjected to self-weight. Three different lengths were tested: (a) $L = 139.9$ mm, (b) $L = 109.9$ mm and (c) $L = 80.5$ mm. The thin red line represents the numerical fit to the mid-plane of the beam with Young's modulus $E_f = 4.27$ MPa.

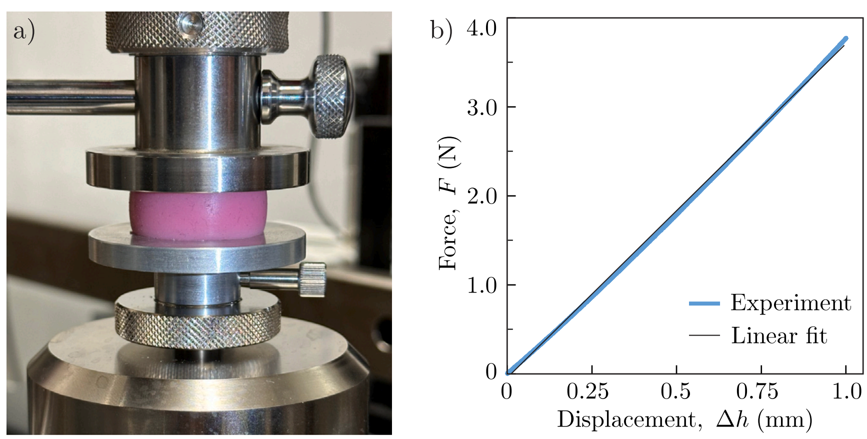

Fig. B.2. Compressive test on the substrate material. (a) Experimental setup and a cylindrical sample made from Zhermack Elite Double 8 (pink color) with the addition of the silicone oil 50% by mass. The diameter and height of the cylindrical specimen were $d = 29.0$ mm and height $h = 12.5$ mm, respectively. (b) Applied force on the cylindrical sample as a function of vertical displacement. Based on the linear fit $F(\Delta h) = 3.7813\Delta h$ a Young's modulus of $E_s = \Delta\sigma/\Delta\varepsilon = 4F(\Delta h)h/(\pi d^2 \Delta h) = 0.072$ MPa is obtained.

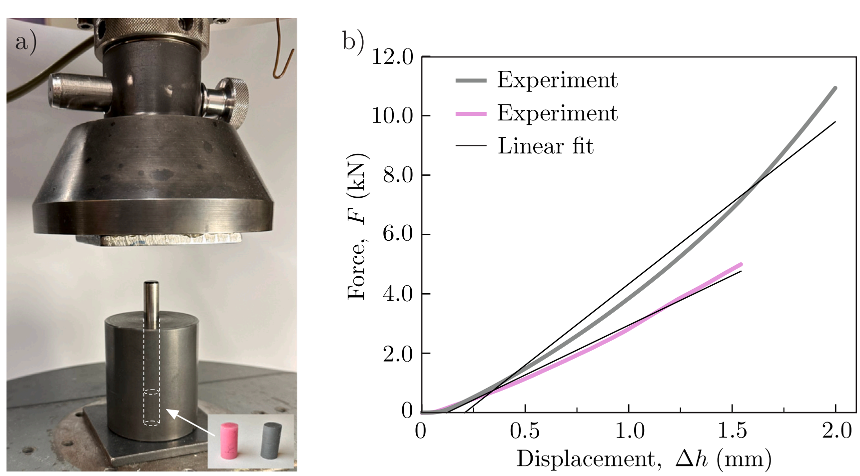

Fig. B.3. Volumetric tests on the film and the substrate materials. (a) Experimental setup and two cylindrical samples made from Zhermack Elite Double 8 (pink color) with the addition of the silicone oil 50% by mass and QSil 550 (gray color) that comprised the substrates and the plates/shells, respectively. (b) Applied force F on the cylindrical sample as a function of vertical displacement for both materials. Based on the linear fit on the measurements $F(\Delta h) = 5467.4\Delta h$ for the gray and $F(\Delta h) = 3353.9\Delta h$ for the pink sample, the Poisson's ratios $\nu_f = 0.4995$ and $\nu_s = 0.4999$ were determined for the respective materials. Both Poisson ratios were determined from the definition of the bulk modulus, $K = -p/\varepsilon_V$, where $p = F/A$, $\varepsilon_V = \Delta V/V$ and from the known relation from linear elasticity $K = E/(3(1-2\nu))$. The symbols A, V and ΔV represent the area of the cross section of the cylindrical sample, the initial volume of the sample and the change in volume. Thus the bulk moduli were $K_f = 1392.3$ MPa and $K_s = 854.1$ MPa for the respective materials.

References

[1] Dinesh Chandra, Shu Yang, Pei Chun Lin, Strain responsive concave and convex microlens arrays, Appl. Phys. Lett. 91 (2007).
[2] Edwin P. Chan, Erica J. Smith, Ryan C. Hayward, Alfred J. Crosby, Surface wrinkles for smart adhesion, Adv. Mater. 20 (2008) 711–716.
[3] Jun Young Chung, Jeffrey P. Youngblood, Christopher M. Stafford, Anisotropic wetting on tunable micro-wrinkled surfaces, Soft Matter 3 (2007) 1163–1169.
[4] D. Terwagne, M. Brojan, P.M. Reis, Smart morphable surfaces for aerodynamic drag control, Adv. Mater. 26 (2014) 6608–6611.
[5] Baolai Jiang, Luntao Liu, Zongpeng Gao, Wenshou Wang, A general and robust strategy for fabricating mechanoresponsive surface wrinkles with dynamic switchable transmittance, Adv. Opt. Mater. 6 (2018).
[6] B. Wei, G. Chen, Q. Wang, A high-performance flexible piezoresistive sensor based on a nanocellulose/carbon-nanotube/polyvinyl-alcohol composite with a wrinkled microstructure, IEEE Sensors J. 22 (2022) 15834–15843.
[7] Gerardo Gutierrez-Heredia, Ovidio Rodriguez-Lopez, Aldo Garcia-Sandoval, Walter E. Voit, Highly stable indium-gallium-zinc-oxide thin-film transistors on deformable softening polymer substrates, Adv. Electron. Mater. 3 (2017).
[8] Michael P. Gaj, Andrew Wei, Canek Fuentes-Hernandez, Yadong Zhang, Radu Reit, Walter Voit, Seth R. Marder, Bernard Kippelen, Organic light-emitting diodes on shape memory polymer substrates for wearable electronics, Org. Electron. 25 (2015) 151–155.
[9] YongAn Huang, Hao Wu, Lin Xiao, Yongqing Duan, Hui Zhu, Jing Bian, Dong Ye, Zhouping Yin, Assembly and applications of 3D conformal electronics on curvilinear surfaces, Mater. Horiz. 6 (2019) 642–683, URL http://dx.doi.org/10.1039/C8MH01450G.
[10] Sun Hong Kim, Sungmook Jung, In Seon Yoon, Chihak Lee, Youngsu Oh, Jae Min Hong, Ultrastretchable conductor fabricated on skin-like hydrogel–elastomer hybrid substrates for skin electronics, Adv. Mater. 30 (2018).
[11] Juliane R. Sempionatto, Muyang Lin, Lu Yin, Ernesto De la paz, Kexin Pei, Thitaporn Sonsa-ard, Andre N. de Loyola Silva, Ahmed A. Khorshed, Fangyu Zhang, Nicholas Tostado, Sheng Xu, Joseph Wang, An epidermal patch for the simultaneous monitoring of haemodynamic and metabolic biomarkers, Nat. Biomed. Eng. 5 (2021) 737–748.
[12] Pietro Ibba, Aniello Falco, Biresaw Demelash Abera, Giuseppe Cantarella, Luisa Petti, Paolo Lugli, Bio-impedance and circuit parameters: An analysis for tracking fruit ripening, Postharvest Biol. Technol. 159 (2020).
[13] Jennie Appel, Mandy L.Y. Sin, Joseph C. Liao, Junseok Chae, Wrinkle cellomics: screening bladder cancer cells using an ultra-thin silicone membrane, ISBN: 9781479935093, 2014, pp. 26–30.
[14] Jiangshui Huang, Megan Juszkiewicz, Wim H. De Jeu, Enrique Cerda, Todd Emrick, Narayanan Menon, Thomas P. Russell, Capillary wrinkling of floating thin polymer films, Science 317 (2007) 650–653.
[15] Siavash Nikravesh, Donghyeon Ryu, Yu Lin Shen, Surface wrinkling versus global buckling instabilities in thin film-substrate systems under biaxial loading: Direct 3D numerical simulations, Adv. Theory Simul. (2022).
[16] Meng Li, Bohua Sun, Post-buckling behaviors of thin-film soft-substrate bilayers with finite-thickness substrate, Sci. Rep. 12 (2022).
[17] Peixia Gu, Xuejun Chen, Role of an interface crack for the blistering mode of a stiff film on a compliant substrate, J. Coatings Technol. Res. 19 (2022) 661–669.
[18] Haohao Bi, Bo Wang, Chao Su, Bohan Zhang, Huajiang Ouyang, Yongan Huang, Zichen Deng, Buckling behaviour of a stiff thin film on a finite-thickness bi-layer substrate, Int. J. Solids Struct. 219–220 (2021) 177–187.
[19] F. Xu, S. Zhao, C. Lu, M. Potier-Ferry, Pattern selection in core-shell spheres, J. Mech. Phys. Solids 137 (2020).
[20] R.C. Liu, Y. Liu, Z. Cai, Influence of the growth gradient on surface wrinkling and pattern transition in growing tubular tissues, Proc. R. Soc. A: Biol. Sci. 477 (2021).
[21] Qiaohang Guo, Shiwen Dou, Nengbin Hua, Chan Zheng, Junjie Lin, Wei Li, Xueqing Xiao, Dinggui Chen, Wenzhe Chen, 3D multi-stable structures with surface wrinkling patterns, Surf. Coat. Technol. 416 (2021).
[22] T. Zhang, Understanding and controlling hexagonal patterns of wrinkles in neo-Hookean elastic bilayer structures, Int. J. Appl. Mech. 13 (2021).
[23] Y. Liu, T. Liang, Y. Fu, Y.X. Xie, Y.S. Wang, A novel buckling pattern in periodically porous elastomers with applications to elastic wave regulations, Extrem. Mech. Lett. 54 (2022).
[24] C. Zhan, M. Wang, H. Li, Z. Wu, Wrinkling of elastic cylinders with material properties varying in radial direction, Front. Mech. Eng. 8 (2022).
[25] Norbert Stoop, Romain Lagrange, Denis Terwagne, Pedro M. Reis, Jörn Dunkel, Curvature-induced symmetry breaking determines elastic surface patterns, Nat. Mater. 14 (2015) 337–342.
[26] F. Xu, M. Potier-Ferry, On axisymmetric/diamond-like mode transitions in axially compressed core-shell cylinders, J. Mech. Phys. Solids 94 (2016) 68–87.
[27] M. Lavrenčič, B. Brank, Hybrid-mixed shell quadrilateral that allows for large solution steps and is low-sensitive to mesh distortion, Comput. Mech. 65 (2020) 177–192.
[28] T. Veldin, B. Brank, M. Brojan, Computational finite element model for surface wrinkling of shells on soft substrates, Commun. Nonlinear Sci. Numer. Simul. 78 (2019) 104863.
[29] T. Veldin, B. Brank, M. Brojan, Discrete Kirchhoff–Love shell quadrilateral finite element designed from cubic Hermite edge curves and coons surface patch, Thin-Walled Struct. 168 (2021) 108268.
[30] Y. Zhao, H. Zhu, C. Jiang, Y. Cao, X.Q. Feng, Wrinkling pattern evolution on curved surfaces, J. Mech. Phys. Solids 135 (2020).
[31] S. Sriram, E. Polukhov, M.A. Keip, Transient stability analysis of composite hydrogel structures based on a minimization-type variational formulation, Int. J. Solids Struct. 230–231 (2021).
[32] B. Brank, J. Korelc, A. Ibrahimbegović, Dynamics and time-stepping schemes for elastic shells undergoing finite rotations, Comput. Struct. 81 (12) (2003) 1193–1210, Advanced Computational Models and Techniques in Dynamics.
[33] M. Lavrenčič, B. Brank, Energy-decaying and momentum-conserving schemes for transient simulations with mixed finite elements, Comput. Methods Appl. Mech. Engrg. 375 (2021) 113625.
[34] M. Lavrenčič, B. Brank, Comparison of numerically dissipative schemes for structural dynamics: Generalized-alpha versus energy-decaying methods, Thin-Walled Struct. 157 (2020) 107075.
[35] B. Brank, J. Korelc, A. Ibrahimbegović, Nonlinear shell problem formulation accounting for through-the-thickness stretching and its finite element implementation, Comput. Struct. 80 (2002) 699–717.
[36] B. Brank, Nonlinear shell models with seven kinematic parameters, Comput. Methods Appl. Mech. Engrg. 194 (2005) 2336–2362.
[37] Zhenyu Huang, Wei Hong, Z. Suo, Evolution of wrinkles in hard films on soft substrates, Phys. Rev. E - Stat. Phys. Plasmas, Fluids, Relat. Interdiscip. Top. 70 (2004) 4.
[38] Z.Y. Huang, W. Hong, Z. Suo, Nonlinear analyses of wrinkles in a film bonded to a compliant substrate, J. Mech. Phys. Solids 53 (2005) 2101–2118.
[39] Xiao Huang, Bo Li, Wei Hong, Yan Ping Cao, Xi Qiao Feng, Effects of tension-compression asymmetry on the surface wrinkling of film-substrate systems, J. Mech. Phys. Solids 94 (2016) 88–104.
[40] Guoxin Cao, Xi Chen, Chaorong Li, Ailing Ji, Zexian Cao, Self-assembled triangular and labyrinth buckling patterns of thin films on spherical substrates, Phys. Rev. Lett. 100 (2008).
[41] Fan Xu, Yangchao Huang, Shichen Zhao, Xi-Qiao Feng, Chiral topographic instability in shrinking spheres, Nat. Comput. Sci. 2 (2022) 632–640.
[42] Jan Zavodnik, Miha Brojan, Spherical harmonics-based pseudo-spectral method for quantitative analysis of symmetry breaking in wrinkling of shells with soft cores, Comput. Methods Appl. Mech. Engrg. 433 (2025) 117529.
[43] T. Veldin, M. Lavrenčič, B. Brank, M. Brojan, A comparison of computational models for wrinkling of pressurized core-shell systems, Int. J. Non-Linear Mech. 4 (2020) 1–5.
[44] M. Lavrenčič, B. Brank, M. Brojan, Multiple wrinkling mode transitions in axially compressed cylindrical shell-substrate in dynamics, Thin-Walled Struct. 150 (2020).
[45] A. Ibrahimbegovic, Nonlinear Solid Mechanics, Springer 1st publication, 2009.
[46] J. Kiendl, M.C. Hsu, M.C.H. Wu, A. Reali, Isogeometric Kirchhoff-Love shell formulations for general hyperelastic materials, Comput. Methods Appl. Mech. Engrg. 291 (2015) 280–303.
[47] J.C. Simo, D.D. Fox, On a stress resultant geometrically exact shell model. Part I: Formulation and optimal parametrization, Comput. Methods Appl. Mech. Engrg. 72 (1989) 267–304.
[48] Wolfram Research, Inc., Mathematica, version 11.3, 2018, Champaign.
[49] J. Korelc, P. Wriggers, Automation of Finite Element Methods, Springer Inter-national Publishing, 2016.
[50] A. Stanić, B. Brank, J. Korelc, On path-following methods for structural failure problems, Comput. Mech. 58 (2016) 281–306.
[51] A. Stanić, B. Brank, A path-following method for elasto-plastic solids and structures based on control of plastic dissipation and plastic work, Finite Elem. Anal. Des. 123 (2017) 1–8.
[52] B. Brank, A. Stanić, A. Ibrahimbegovic, A path-following method based on plastic dissipation control, in: Adnan Ibrahimbegovic (Ed.), Computational Methods for Solids and Fluids: Multiscale Analysis, Probability Aspects and Model Reduction, Springer International Publishing, Cham, 2016, pp. 29–47.
[53] R. Lagrange, F. Lopez Jimenez, D. Terwagne, M. Brojan, P.M. Reis, From wrinkling to global buckling of a ring on a curved substrate, J. Mech. Phys. Solids. 89 (2016) 77–95.
[54] A. Lee, P.T. Brun, J. Marthelot, G. Balestra, F. Gallaire, P.M. Reis, Fabrication of slender elastic shells by the coating of curved surfaces, Nat. Commun. 7:11155 (2016).
[55] M. Brojan, D. Terwagne, R. Lagrange, P.M. Reis, Wrinkling crystallography on spherical surfaces, Proc. Natl. Acad. Sci. USA 112 (1) (2015) 14–19.
[56] J. Dujc, B. Brank, Stress resultant plasticity for shells revisited, Comput. Methods Appl. Mech. Engrg. 247–248 (2012) 146–165.